DRAFT VERSION AUGUST 23, 2013
Preprint typeset using LaTeX style emulateapj v. 5/2/11

CONFIRMATION VIA THE CONTINUUM-FITTING METHOD THAT THE SPIN OF THE BLACK HOLE IN CYGNUS X-1 IS EXTREME

LIJUN GOU[1,2] JEFFREY E. MCCLINTOCK[2], RONALD A. REMILLARD[3], JAMES F. STEINER[2], MARK J. REID[2], JEROME A. OROSZ[4], RAMESH NARAYAN[2], MANFRED HANKE[5], AND JAVIER GARCÍA[2]

Draft version August 23, 2013

ABSTRACT

In Gou et al. (2011), we reported that the black hole primary in the X-ray binary Cygnus X-1 is a near-extreme Kerr black hole with a spin parameter $a_* > 0.95$ (3σ). We confirm this result while setting a new and more stringent limit: $a_* > 0.983$ at the 3σ (99.7%) level of confidence. The earlier work, which was based on an analysis of all three useful spectra that were then available, was possibly biased by the presence in these spectra of a relatively strong Compton power-law component: The fraction of the thermal seed photons scattered into the power law was $f_{\rm s} = 23 - 31\%$, while the upper limit for reliable application of the continuum-fitting method is $f_{\rm s} \lesssim 25\%$. We have subsequently obtained six additional spectra of Cygnus X-1 suitable for the measurement of spin. Five of these spectra are of high quality with $f_{\rm s}$ in the range 10% to 19%, a regime where the continuum-fitting method has been shown to deliver very reliable results. Individually, the six spectra give lower limits on the spin parameter that range from $a_* > 0.95$ to $a_* > 0.98$, allowing us to conservatively conclude that the spin of the black hole is $a_* > 0.983$ (3σ).

Subject headings: X-rays:binaries – black hole physics – binaries:individual (Cygnus X-1)

1. INTRODUCTION

The X-ray binary Cygnus X-1 was discovered in the early days of X-ray astronomy (Bowyer et al. 1965), and its compact primary was the first black hole candidate to be established via dynamical observations (Webster & Murdin 1972; Bolton 1972). Recently, in three sequential papers on Cygnus X-1, we reported accurate values of the source distance D (Reid et al. 2011), black hole mass M and orbital inclination i (Orosz et al. 2011), and an extreme value for the black hole's spin parameter, $a_* > 0.95$ ($3\,\sigma$; Gou et al. 2011)[6].

We measured the spin of the black hole by fitting the thermal X-ray continuum spectrum of the accretion disk to the thin-disk model of Novikov & Thorne (1973). The key fit parameter is the radius of the inner edge of the accretion disk, which is equivalent to the radius of the innermost stable circular orbit $R_{\rm ISCO}$ (Zhang et al. 1997; McClintock et al. 2013). In turn, $R_{\rm ISCO}/M$ is directly related to the dimensionless spin parameter a_* (Bardeen et al. 1972). The continuum-fitting method of measuring spin is simple: It is strictly analogous to measuring the radius of a star whose flux, temperature and distance are known. By this analogy, it is clear that one must have accurate estimates of D, M and i in order to obtain an accurate estimate of a_* by fitting the X-ray spectrum. The robustness of the continuum-fitting method is demonstrated by the dozens or hundreds of independent and consistent measurement of spin that have been obtained for several black holes (e.g., Steiner et al. 2010), and through careful consideration of many sources of systematic errors (e.g., Steiner et al. 2011; Kulkarni et al. 2011; Zhu et al. 2012).

Herein, using the continuum-fitting method (McClintock et al. 2013) and precisely the same methodologies that are described in Gou et al. (2011; hereafter GOU11) – but using data of much higher quality – we confirm our conclusion that Cygnus X-1's black hole is a near-extreme Kerr hole, a result that has received support via the independent Fe-line method of measuring spin (see Section 7.1). Importantly, these new data allow us to obtain a more stringent limit on the spin parameter, namely, $a_* > 0.98$ ($3\,\sigma$).

For reliable application of the continuum-fitting method, it is essential that the thermal disk component dominate over the Compton power-law component (McClintock et al. 2013), which is always present in the spectra of X-ray binaries. It is by this criterion that the present data are of much higher quality than those analyzed in GOU11, as we now explain. The strength of the complicating Compton component is parameterized by the scattering fraction $f_{\rm s}$, which is the fraction of the thermal seed photons scattered into the power-law component (Steiner et al. 2009b). Ideally, $f_{\rm s}$ is a few percent, while the limit for reliable application of the continuum-fitting method, based on a thorough investigation of two black hole binaries, has been shown to be $f_{\rm s} \lesssim 25\%$ (Steiner et al. 2009a). The extreme spin reported in GOU11 is based on an analysis of the only three spectra of Cygnus X-1 that were then available and suitable for measurement of spin via the continuum-fitting method. One spectrum was marginally within the limit ($f_{\rm s} = 23\%$) and the other two were above the limit (both with $f_{\rm s} = 31\%$). Herein, we report on spin results for six new spectra, five of which have much more favorable scattering fractions in the range $f_{\rm s}$ =10%-19%. Each of the six spectra individually confirms the spin limit set by GOU11 ($a_* > 0.95$ at 3σ).

It is challenging to measure the spin of Cygnus X-1 not only because the Compton component is always relatively strong for this source (e.g., see Section 4.3 in

[1] National Astronomical Observatory, Chinese Academy of Science, Beijing, 100012, China
[2] Harvard-Smithsonian Center for Astrophysics, Cambridge, MA, 02138, USA
[3] Kavli Institute for Astrophysics and Space Research, MIT, 70 Vassar Street, Cambridge, MA, 02139, USA
[4] Department of Astronomy, San Diego State University, 5500 Campanile Drive, San Diego, CA, 92182, USA
[5] Remeis-Observatory & ECAP, University of Erlangen-Nuremberg, Sternwartstr. 7, 96049 Bamberg, Germany

[6] The dimensionless spin parameter $a_* \equiv cJ/GM^2$ with $|a_*| \leq 1$, where J is the angular momentum of the black hole.

McClintock & Remillard 2006), but also for two additional reasons: (1) It is essential to have spectral data that span a broad energy range, $\sim 0.5 - 40$ keV, in order to simultaneously constrain the unusually soft thermal component ($kT \sim 0.5$ keV) and the Compton power-law and reflected components (see Section 2 and Figure 3 in GOU11), and such broadband data are rare; and (2) the source usually dwells in its soft state only about 10% of the time (see Figure 1 in GOU11). In mid-2010, Cygnus X-1 again entered the soft state. Seizing this opportunity, we observed the source with *Chandra*, *Swift*, *Suzaku*, and *RXTE* and obtained the spectra with moderate values of $f_{\rm s}$ that are mentioned above. The times of these various observations are indicated by arrows in the X-ray light curve shown in Figure 1.

The paper is organized as follows: In Section 2, we describe the observations and data reduction, and in Section 3 the data analysis and our spectral model. Presented in Sections 4, 5 and 6 respectively are our results, a discussion of their robustness, and a comprehensive analysis of the errors. We discuss two topics in Section 7 and offer our conclusions in the final section.

2. OBSERVATIONS AND DATA REDUCTION

In late 2010 and during 2011, we made the five soft-state observations listed in Table 1 using *Chandra*, *Swift*, *Suzaku* and *RXTE*. For the four *Chandra* and *Swift* observations, the essential high-energy coverage was provided via simultaneous observations made using the Proportional Counter Array (PCA) aboard *RXTE*. Because *RXTE* observations are segmented by Earth occultations and because we require that the *RXTE* observations be strictly simultaneous (with those of *Chandra* or *Swift*), we chopped the five observations into ten observation intervals, each providing one of the spectra S1–S10 that are listed in Table 1. Here and throughout, "spectrum" refers to a segment of an observation, as schematically defined in Table 1. While two spectra may be part of a single contiguous observation, any two observations were obtained at disjoint time intervals and correspond to distinct pointings. We adhere to this language throughout.

Observation No. 1, which corresponds to spectra S1–S5 (Table 1), is by far the most important observation because the Compton component is relatively faint, much fainter than during Observations 2–5, and also much fainter than during the three observations reported on in GOU11. For this crucial observation, we show in Figure 2 the count rates measured by *RXTE* and *Chandra*.

We now discuss in turn the observations and data reduction procedures for *Chandra* and *Swift*, and then for *RXTE*, which provides the complementary high-energy coverage. In the final subsection, we discuss Observation No. 5, which was performed solely by *Suzaku*, with the high-energy coverage provided by *Suzaku*'s Hard X-ray Detector (HXD). Table 1 gives for each observation basic information including the energy range used in analyzing the data for a given detector, the gross observation times, the effective exposure times, the intensity of the source in Crab units, the spectral hardness (Figure 1) and the orbital phase of the binary system. The orbital phase is useful for assessing the likelihood that an observation is affected by absorption dips, which are observed in both the hard and soft states of Cygnus X-1 near phase zero (e.g., Hanke et al. 2009; Yamada et al. 2013).

2.1. *Obs. No. 1: Chandra – Continuous Clocking (CC)*

This key observation (ObsID=12472) was obtained in the ACIS CC mode. As indicated in Figure 2 and discussed above, the observation, which has a total duration of 24 ks, was parceled up into five data segments. The start and stop times for each data segment, which are given in Table 1, are the same as those for the corresponding *RXTE* PCA observation (Figure 2). The individual PCA observation times range from 1.5 ks to 3.4 ks, while the corresponding *Chandra* net exposure times are ≈ 4 times shorter (Table 1).

For this *Chandra* observation, as well as for Observation No. 2 (Section 2.2), we (i) used the High-Energy Transmission Grating (HETG) and the Advanced Camera for Imaging and Spectroscopy (ACIS-S; Canizares et al. 2005; Garmire et al. 2003); (ii) binned the data to achieve a minimum number of counts per channel of 200[7]; and (iii) made no allowance for systematic error because the statistical error is large.

The data-rate limitation of the CCD detectors makes it challenging to observe a bright and variable source like Cygnus X-1. The principal problem is "pile-up," i.e., the registering of two or more photons in the same or adjacent pixels within a single frame time. In the CC mode, the frame time is reduced to 2.85 ms by continuously transferring the data from the image array to the frame-store array. While this essentially eliminates pile-up, the details of the spatial distribution in the columns are then lost due to the collapse of the 2D image into a 1D image. In order to avoid saturating the telemetry, only the data for the High Energy Grating (HEG; -1 order) and Medium Energy Grating (MEG; +1 order) components of the HETG were transmitted. The spectra were extracted following the standard procedures[8]. We fitted these data over the full energy range 0.5–10.0 keV (except for the 1.3–2.0 keV chip gap in the MEG spectrum).

2.2. *Obs. No. 2: Chandra – Timed Exposure (TE)*

In reducing these TE-mode (ObsID=13219) data, we followed the method described by Smith et al. (2002). Again, only the orders of the HEG and MEG spectra mentioned above were used. In addition, for the TE mode the data for the readout streak on the same side of the HEG and MEG spectra were also used. We extracted the "streak" and background spectra following the recommended procedures[9]. Although the net exposure times for the two TE-mode spectra S6 and S7 are respectively 3.6 ks and 0.9 ks, the effective exposure times for the streak spectra are only about 19.2 s and 5.0 s, respectively. For these streak spectra, we estimate that less than 5% of the events are affected by pileup, and we therefore use the full 0.5–10 keV bandwidth. For the dispersed grating spectrum, we only included data for which $< 5\%$ of the events are piled up; for the HEG and MEG respectively these data are in the energy ranges 0.7–0.9 keV and 7.0–10.0 keV.

2.3. *Obs. Nos. 3–4: Swift – Windowed Timing (WT)*

Three *Swift/RXTE* observations were performed on UT October 8, 24 and 26. We disregard the observation of October 24 because the *RXTE* data were not simultaneous and

[7] The bin size used is approximately 2–4 times larger than the default grating resolution, as recommended for modeling the continuum http://cxc.harvard.edu/ciao/threads/spectra_grouping/. The fit results are unchanged if the data are binned more finely, although reduced chi-squared will be slightly lower.

[8] http://cxc.harvard.edu/ciao/threads/spectra_hetgacis/

[9] http://cxc.harvard.edu/ciao/threads/streakextract/

the source was highly variable during this period. The WT mode was used to minimize the effects of pile-up. The data were extracted using the procedures outlined in Romano et al. (2006)[10]. We used an extraction aperture of 50×20 pixels for the background region and typically 40×20 pixels for the source region (40 pixels long along the image strip and 20 pixels wide; 1 pixel=2.36 arcsec). Despite our use of the WT mode, the data are strongly affected by pile-up. According to the observation manual[11], pile-up is negligible below 300 counts s^{-1}; however, the count rate exceeded 800 counts s^{-1} for all of our observations. We therefore excluded a 15×20 pixel region in the center of the source extraction region to ensure that pileup effects remain under 5%.

We netted three simultaneous observations, each > 1 ks in duration (Table 1), that we use to measure spin. Although the gap between the two observations is only ≈ 30 min, we chose not to combine them because our model fits show strong source variability, with the source intensity increasing from 0.59 Crab to 0.90 Crab (Table 1) and the scattering fraction increasing from 31% to 50% (Section 3). All the *Swift* data were binned to achieve a minimum number of counts per channel of 200, and we included a systematic error of 0.5% in the count rates in each PHA channel.

2.4. *Obs. Nos. 1–4: RXTE*

As in GOU11, for *RXTE* we elected to use only the data from what historically has been the best-calibrated detector, PCU2. Meanwhile, it is unimportant whether one uses PCU2 alone or all the PCUs (GOU11). All the *RXTE* spectra have been reprocessed using the latest PCA calibrations available in NASA software release HEAsoft 6.13. In particular, we generated new response files and used the latest assignments for converting pulse-height channel to energy. In addition, we used a revised PCA background model, "pca_bkgd_cmvle_eMv20111129.mdl", which we obtained from the PCA instrument team. Furthermore, we corrected the effective area of the PCA using the Toor & Seward (1974) spectrum of the Crab Nebula precisely as described in Section 2 in GOU11, thereby obtaining for Observation Nos. 1/2/3/4 normalization correction factors $C_{\rm TS}$ of 1.128/1.133/1.123/1.123 and a correction to the slope of the power law of $\Delta\Gamma_{\rm TS}$ 0.022/0.024/0.023/0.023; the respective dead time correction factors are 1.029/1.039/1.048/1.048. Finally, as customary for PCA observations of bright sources, we included an allowance of 0.5% for systematic error. We fitted the *RXTE* spectra over the energy range 2.9–50 keV (pulse-height channels 4 to 83).

2.5. *Obs. No. 5: Suzaku*

Both the X-ray Imaging Spectrometer (XIS) and the Hard X-ray Detector (HXD) were used for this observation with a gross observing time of ≈ 5 ks (Table 1). We reduced the data using the standard procedures described in Yamada et al. (2012). There is no fast readout mode for the XIS detector, and the effects of pile-up are large, even though we excluded the counts in the central source region within a radius of 60 pixels. To achieve an acceptable fit (χ^2 <2.0), for the XIS we ignored the energy ranges: 1.7–1.9 keV and 2.1–2.3 keV, and for the HXD we ignored the energy range below 20 keV. We furthermore added the 2% customary systematic error for the XIS. (No systematic error was included for the HXD.) Given (1) that the fit we were able to achieve is relatively poor with $\chi^2_\nu = 1.69$, (2) the lack of any constraint on the reflection component in the 10–20 keV band, and (3) the significant effects of pile-up we do not use the *Suzaku* spectrum to estimate spin, although for completeness we list the observation in Table 1.

[10] see also http://www.swift.ac.uk/analysis/xrt/pileup.php

[11] http://www.swift.ac.uk/pileupthread.shtml

3. DATA ANALYSIS

A soft-state spectrum of Cygnus X-1 is comprised of thermal, power-law and reflected components, which are illustrated in Figure 3. The latter component includes the Fe Kα emission line. A schematic sketch of the physical structures that give rise to the three spectral components, namely the accretion disk and the corona, are shown in Figure 2 in GOU11.

The data analysis and model fitting throughout this paper were performed using XSPEC[12] version 12.6.0 (Arnaud 1996) and, unless otherwise indicated, errors are everywhere reported at the 1σ level of confidence. In this section and the following one, we fix the input parameters D, i and M at their fiducial values (see Section 4).

In GOU 11, we analyzed three spectra of Cygnus X-1 by working in detail through a progression of seven preliminary models. The first three models, NR1–NR3, were non-relativistic, with the accretion disk component modeled using DISKBB. The results for the physically most realistic of these models, NR3, were gratifying: We obtained very consistent values of inner-disk temperature and radius for the three spectra ($T_{\rm in} = 0.532, 0.539$ and 0.543 keV and $R_{\rm in} = 2.06, 2.30$ and $2.01\ GM/c^2$; see Table 7 in GOU11).

Next, we analyzed the spectra using four preliminary relativistic models, R1–R4, which are built around the fully relativistic accretion-disk model component KERRBB2 (McClintock et al. 2013). This component is a direct replacement for DISKBB, returning two fit parameters, namely a_* and the mass accretion rate $\dot{M}$ (instead of temperature and inner-disk radius). These four models progress toward our adopted model in the sense that R1 is the most primitive and our adopted model the most physically realistic. All four models and our adopted model gave very similar results for the parameter of interest, namely a_*. We chose to present in detail our results for models R1–R4 in order to demonstrate that our modeling of the critical thermal component – and the extreme spin it delivers for Cygnus X-1 – are insensitive to the details of the analysis, as expected given the dominance of the thermal component.

In this paper, we employ a single model, namely the one adopted in GOU11, which is the most accurate of the eight models considered by GOU11. Its structure, naming all the components that comprise it, is expressed as follows:

$$\mathrm{CRABCOR} * \mathrm{CONST} * \mathrm{TBABS}\ [\mathrm{SIMPLR} \otimes \mathrm{KERRBB2} + \mathrm{KERRDISK} + \mathrm{KERRCONV} \otimes (\mathrm{IREFLECT} \otimes \mathrm{SIMPLC})]$$

As described in more detail below, SIMPLR generates the power-law component using the seed photons supplied by the thermal component KERRBB2, while the reflection component is likewise generated in turn by IREFLECT acting solely on the power-law component (i.e., IREFLECT does not act on the thermal component). The fit returns a single value of a_*, which is a key fit parameter in three of the model components: KERRBB2, KERRDISK and KERRCONV. We now dis-

[12] XSPEC is available at http://heasarc.gsfc.nasa.gov/xanadu/xspec/

cuss in turn the model's three principal components – thermal, power-law and reflected – and their interrelationships.

Thermal component: The centerpiece of our adopted model is the accretion-disk model component KERRBB2, which includes all relativistic effects, self-irradiation of the disk ("returning radiation") and limb darkening (Li et al. 2005; McClintock et al. 2013). The effects of spectral hardening are incorporated into the basic model KERRBB via a pair of look-up tables for the hardening factor f corresponding to two representative values of the viscosity parameter: $\alpha = 0.01$ and 0.1. Throughout this work we use $\alpha = 0.1$ unless stated otherwise (King et al. 2007). The entries in the look-up tables for f were computed using both KERRBB and a second relativistic disk model BHSPEC (Davis et al. 2005; Davis & Hubeny 2006). We refer to the model KERRBB plus this table, and the subroutine that reads it, as KERRBB2 (McClintock et al. 2013). As noted above, the model KERRBB2 has just two fit parameters, namely, the black hole spin parameter a_* and the mass accretion rate $\dot{M}$ (or equivalently, a_* and the Eddington-scaled bolometric luminosity of the disk, $L(a_*, \dot{M})/L_{\rm Edd}$). In computing the results reported in this paper (and in GOU11), we included the effects of limb darkening and returning radiation. We set the torque at the inner boundary of the accretion disk to zero, fixed the normalization to 1, (as appropriate when D, M and i are held fixed), allowed the mass accretion rate to vary freely, and fitted directly for the spin parameter a_*.

Power-law component: The first term in square brackets, SIMPLR⊗KERRBB2, models the power-law component and the observed thermal component in combination. This dominant part of the spectrum (see Figure 3) is computed by convolving KERRBB2, which describes the seed photon distribution (i.e., the thermal component prior to being scattered), with SIMPLR. The convolution model SIMPLR (Steiner et al. 2011) is a slightly modified version of SIMPL (Steiner et al. 2009b) that is appropriate for use in conjunction with an additive reflection component (Steiner et al. 2009b). The two key parameters of SIMPLR (and SIMPL) are the power-law photon index Γ and the scattered fraction $f_{\rm s}$ (Steiner et al. 2009b). SIMPLR has one additional parameter that specifies the fraction of the power-law photons that strike the disk (Steiner et al. 2011). As used here, SIMPLR describes a corona that sends half the scattered seed photons outward toward the observer and the remainder downward toward the disk, thereby generating the reflected component. That is, we assume that the power-law component illuminating the disk is the same as the component we observe.

Reflected component: The second and third additive terms in square brackets model the reprocessed emission from the disk. The reflected component results from the disk's response to the illuminating power-law component described by SIMPLC, the isolated Compton component as seen by the disk (Steiner et al. 2011). SIMPLC is equivalent to SIMPLR⊗KERRBB2 minus the unscattered portion of the thermal component. SIMPLC is in turn acted on by IREFLECT, which is a convolution reflection model with the same properties as its widely-used parent, the additive reflection model PEXRIV (Magdziarz & Zdziarski 1995). We everywhere adopt solar abundances; link the photon index to the value returned by SIMPLR; and fix the disk temperature at 6.0×10^6 K, the temperature $T_{\rm in}$ returned by DISKBB; and set the scaling factor s in IREFLECT to negative unity[13] (see GOU11 for details). The model IREFLECT⊗SIMPLC returns a reflected spectrum that contains sharp absorption features and no emission lines. To complete the model of the reflected component, we follow Brenneman & Reynolds (2006) and employ the line model KERRDISK and the convolution smearing model KERRCONV, both of which treat a_* as a free fit parameter[14]. These latter two models allow the emissivity indices to differ in the inner and outer regions of the disk. For simplicity, and because this parameter is unknown with values that vary widely from application to application, we use an unbroken emissivity profile with a single index q. We tie together all the common parameters of KERRDISK and KERRCONV, including the two principal parameters, namely a_* and q.

The three multiplicative model components are (1) CRABCOR, which corrects for calibration deviations relative to Toor & Seward (see Section 2 in GOU11 and Steiner et al. 2011); (2) CONST, which reconciles the calibration differences between the detectors (throughout the paper, we fix the normalization of the *RXTE*/PCU2 detector to unity and fit for the normalization of the *Chandra* and *Swift* detectors); and (3) TBABS[15], a standard low-energy absorption model (Wilms et al. 2000).

Comparing Figure 3 with the corresponding Figure 3 in GOU11, one sees at a glance that spectra S1–S5 (with $f_{\rm s} = 10 - 19\%$) are much more strongly disk-dominated than spectra SP1–SP3 in GOU11 (with $f_{\rm s} = 23 - 31\%$). For spectra S1–S5, the peak flux in the thermal component is 5–10 times the peak flux in the power-law component, and it is ≈ 25 times the peak flux in the reflected component. As we discuss in the conclusion section of the paper (Section 8), spectra S1–S5 (Figure 3) are of the same quality as spectra that delivered reliable values of spin for the black hole primaries in XTE J1550–564 (Steiner et al. 2011) and H1743–322 (Steiner et al. 2012).

4. RESULTS

In this section, we present results with the key input parameters fixed at their fiducial values: $D = 1.86$ kpc, $M = 14.8\ M_\odot$, and $i = 27.1$ deg (Reid et al. 2011; Orosz et al. 2011). The fit results for all ten spectra, S1–S10, are summarized in Tables 2 and 3.

Before broadly discussing the results, we focus on the value of the scattering fraction, $f_{\rm s}$ (Tables 2 and 3), and we strictly follow the data selection criterion $f_{\rm s} \lesssim 25\%$ (Steiner et al. 2009a). Therefore, we henceforth consider only the six spectra S1–S6 for which $f_{\rm s} \leq 24\%$, and we disregard the remaining spectra (S7–S10). Before doing so, we note that the results for spectra S7–S10 are, in detail, reasonably consistent with those of the six selected spectra. We furthermore note that the values of $f_{\rm s}$ for three of the rejected spectra (S7, S8 and S10) are very nearly the same as for the two inferior spectra used in GOU11 (SP2 and SP3), namely $f_{\rm s} \approx 30\%$.

We now direct our attention solely to spectra S1–S6 with values of $f_{\rm s} = 10 - 24\%$. The fits are all good, with χ^2_ν ranging from 0.95 to 1.40. The spin parameter is very high

[13] Corresponds to isotropic emission, where the negative sign means that only the reflected component is calculated.

[14] Our results are essentially unchanged if we instead use RELLINE and RELCONV (Dauser et al. 2010).

[15] The updated model TBnew, which improves the resolution of the absorption cross sections of the elements at low energies (typically less than 0.9 keV), will not affect the results. The details can be found at http://pulsar.sternwarte.uni-erlangen.de/wilms/research/tbabs/

and is pinned at the $a_* = 0.9999$ limit of the KERRBB2 model (McClintock et al. 2013), which is the principal result of this section.

The luminosity of the disk component is low and uniform, $L/L_{\rm Edd} = 1.9 - 2.2\%$, and it easily meets a key data selection criterion for successful application of the continuum-fitting method, namely $L/L_{\rm Edd} < 30\%$ (McClintock et al. 2006, 2013). Correspondingly, the disk is expected to be geometrically very thin at all radii (with aspect ratio $h/r < 0.05$; see Penna et al. 2010; Kulkarni et al. 2011; Zhu et al. 2012). At the same time, the luminosity is sufficiently high that the spectral hardening factor f is well-determined ($f \approx 1.6$).

The column density is statistically well determined with uncertainties of only 1–2% [16], while it varies by 3.3% (std. deviation; N=6). This is as expected since $N_{\rm H}$ is known to vary by several percent for all three well-studied supergiant black-hole binaries, namely, Cygnus X-1 (Hanke et al. 2009), M33 X-7 (Liu et al. 2008) and LMC X-1 (Hanke et al. 2010). The power-law slope is well determined and quite stable, $\Gamma = 2.52 \pm 0.12$ (std. deviation; N=6), and its value is the expected one for the steep power-law state ($\Gamma > 2.4$; Remillard & McClintock 2006). The ionization parameter is modest and in the range $\xi \approx 70 - 170$.

5. ROBUSTNESS OF SPIN ESTIMATES

In GOU11, we discuss many factors that might affect our key result, namely the extreme spin of Cygnus X-1; we find that none of them are significant. Here, we review these matters briefly. For further details, see Sections 5 and 7 in GOU11, and also see Section 5 in McClintock et al. (2013). Sections 5.4 and 5.5 below are wholly new and discuss our adopted reflection model in relation to the recently-released reflection model XILLVER (García et al. 2013). Section 5.8 on the effect of dust scattering is likewise new.

5.1. *Errors from the Novikov-Thorne Model*

The accuracy of continuum-fitting results ultimately depends on the reliability of the Novikov-Thorne model. The key assumption of this model is that the torque, and hence the flux, vanishes at the ISCO (Shafee et al. 2008a; Penna et al. 2010). The effects of this approximation on spin measurements have been quantitatively investigated via general relativistic magnetohydrodynamic (GRMHD) simulations of thin disks by several authors (Noble et al. 2011; Kulkarni et al. 2011; Zhu et al. 2012). The general consensus is that the zero-torque approximation introduces uncertainties in spin estimates of around $\Delta a_* \sim 0.1$ for low spin values ($a_* < 0.5$) and much smaller errors as $a_* \to 1$. These error estimates, which are for geometrically thin disks ($H/R \approx 0.05$, or $L/L_{\rm Edd} \sim 0.35$) are in practice less than the observational errors in the parameters D, M and i. For more details concerning the Novikov-Thorne model and a discussion of other sources of model errors, see Section 5 in McClintock et al. (2013).

5.2. *Effect of Iron Line and Edges*

In GOU11, we showed that the Fe-line and other reflection features in soft-state spectra of Cygnus X-1 are cosmetic and have a negligible effect on the continuum-fitting measurement of spin. Specifically, we refitted the three spectra considered in GOU11 excluding the 5.0-10.0 keV band and the Fe-line component KERRDISK. This excised the energy range containing the relativistically broadened Fe Kα line and edge, as well as a significant residual feature near 9 keV [17]. We found that our spin results were essentially unchanged, as expected given the modest equivalent widths of these features.

5.3. *Effect of Extending the Bandwidth to 150 keV*

In Section 5.2 of GOU11, it is argued that the coverage of the PCA to 45 keV is sufficient to constrain the power-law and reflection components; we demonstrated that this is true by refitting one of the spectra including the *RXTE* HEXTE data, which span the energy range 20 keV to 150 keV. This result is unsurprising given that the PCA coverage to 45 keV is more than adequate to determine the power-law component, while the reflection component is dying rapidly at 45 keV (Figure 3).

5.4. *Effect of using a Different Reflection Model*

As in Section 5.3 in GOU11, we replaced our reflection component KERRCONV⊗IREFLECT⊗SIMPLC+KERRDISK with KERRCONV⊗REFLIONX, which is widely used in measuring spin via the Fe Kα line. As in GOU11, we again find that the effects on the spin parameter are essentially nil. More recently, a new and improved reflection model XILLVER has become available (García et al. 2013). This version of XILLVER (like REFLIONX) is intended for use when the thermal disk flux is faint compared to the incident power-law flux, and it is therefore not well-suited to our case. Nevertheless, as with REFLIONX, we performed a test by replacing our reflection component with KERRCONV⊗XILLVER. The fits are poorer with reduced chi-square ranging from 1.8 to 2.2, but the effects on the spin parameter were again found to be quite negligible.

5.5. *On the Accuracy of our Adopted Reflection Model*

In computing the reflected component, we rely on IREFLECT, a convolution model with the same properties as its widely used parent, the additive model PEXRIV, which returns a spectrum that contains sharp absorption lines and no emission lines. Figure 20 in García et al. (2013) shows that (ignoring line emission) IREFLECT/PEXRIV is a good approximation to the sophisticated model XILLVER at low ionization, $\xi = 1$ (left panel), while it is a very poor approximation at high ionization, $\xi = 10^3$ (right panel). In Figure 4, we show that for an intermediate case, $\xi \sim 10^2$, which corresponds to the moderately ionized disk of Cygnus X-1 (see Tables 2 and 3), IREFLECT/PEXRIV is in reasonable agreement with XILLVER. Considering further that the peak reflected flux is ≈ 25 times fainter than the peak thermal flux (Figure 3), it is not surprising that our estimate of spin is insensitive to the choice of reflection model.

In all the fits we have fixed the disk temperature in the reflection model at 6.0×10^6 K, which corresponds to 0.52 keV. The disk temperature is quite constant for all the spectra considered here and in GOU11 near this value ($kT \approx 0.54$ keV; Section 3). Meanwhile, increasing the disk temperature by 50% to 9.0×10^6 K or halving it has a negligible effect on

[16] The average value of $N_{\rm H}$, $(0.754 \pm 0.016) \times 10^{22}$ cm^{-2}, agrees very well with the values derived from the 21-cm line in the direction of Cygnus X-1, which is $N_{\rm H} = 0.721 \times 10^{22}$ cm^{-2}, a weighted average from both LAB and DL maps (Kalberla et al. 2005; Dickey & Lockman 1990).

[17] This feature results from the imperfect performance of IREFLECT/PEXRIV (Section 3), the reflection model we employ. The limitations of this model, which are well known (Ross et al. 1999; García et al. 2013), are discussed in Section 5.5, while the model's marginal performance near the Fe edge is illustrated in Figure 4.

the spin and other key parameters (apart from the ionization parameter).

5.6. *Effect of Varying the Viscosity Parameter and Metallicity*

Refitting the spectra using $\alpha = 0.01$ in place of our fiducial value ($\alpha = 0.1$) has a very slight effect, and doing so only increases the already extreme value of spin. The effects of varying metallicity are likewise very small, whether one grossly decreases its value to a tenth solar or considers the suprasolar values implied by the IREFLECT fits (Tables 1 and 2). In the former/latter case, the spin is depressed/increased, but only very slightly (see Section 5.4 in GOU11). An analysis of high resolution optical spectra of the donor star indicates that Fe is somewhat overabundant relative to solar (Karitskaya et al. 2007).

5.7. *Effect of a Warm Absorber*

Although careful modeling of warm absorbers is usually crucial in determining the spins of supermassive black holes via the Fe Kα method (e.g., Brenneman & Reynolds 2006), we showed via an analysis of *Chandra* HETG spectra that their effects are unimportant in estimating the spin of Cygnus X-1 via the continuum-fitting method (see Section 7.6 in GOU11).

5.8. *Effect of Dust Scattering*

The dust scattering halo of Cygnus X-1 (e.g., Xiang et al. 2011) has an effect on the source spectrum that is equivalent to direct absorption. In order to assess the effects of dust scattering on our results, we used the only relevant model that is presently available in XSPEC, namely DUST. The model assumes that the source flux is scattered into a uniform disk whose size and total flux vary respectively as $1/E$ and $1/E^2$. The simple model DUST is a good approximation to more accurate models (e.g., Weingartner & Draine 2001) at energies in the bandpass of interest, namely $E > 0.8$ keV (Table 1).

We reanalyzed spectra S1–S5 as before, but this time we included the multiplicative model component DUST. The model has two parameters that specify at 1 keV (1) the fraction of photons scattered by dust grains, and (2) the size of the halo in units of the detector beam size. If both parameters are allowed to vary, neither can be constrained. We therefore initially fixed the scattering parameter to 0.17, which was obtained by extrapolating the value 0.12 at 1.2 keV given by Predehl & Schmitt (1995, see their Figure 10). The results obtained for the key parameters a_* and $f_{\rm s}$ for each of the five spectra are essentially identical to those that appear in Table 2, although the column density $N_{\rm H}$ is reduced by $\approx 13\%$. Even if one increases the dust scattering parameter from 0.17 to 0.3, the values of a_* and $f_{\rm s}$ are essentially unchanged, while in this case $N_{\rm H}$ is reduced by $\approx 25\%$. We conclude that the effects of dust scattering are unimportant.

5.9. *Effect of a Possible Spin-Orbit Misalignment*

In Section 7.4 in GOU11, we considered a principal source of uncertainty in the continuum-fitting method, namely, whether the inner X-ray emitting portion of the disk (which for a thin disk will align with the black hole's spin axis) is aligned with the binary orbital plane. If, as some evidence suggests, the persistent supergiant systems are formed by direct, kickless collapse (Mirabel & Rodrigues 2003; Reid et al. 2011), then spin-orbit alignment would be expected for these systems. (For full discussions on the topic of spin-orbit alignment, see Section 1 in Steiner et al. 2012, and Section 5.4 in McClintock et al. 2013). In any case, as we demonstrate for Cygnus X-1 in Figure 5 in GOU11, even if there exists a misalignment angle as large as, e.g., 16 deg, the spin value is still $>$0.95 (ignoring the uncertainties in D, M and i).

6. COMPREHENSIVE ERROR ANALYSIS

The dominant error in all continuum-fitting measurements of spin is attributable to the observational uncertainties in the source distance, black hole mass and disk inclination. For Cygnus X-1, we have determined accurate values for these quantities: $D = 1.86^{+0.12}_{-0.11}$ kpc (Reid et al. 2011), $M = 14.8 \pm 1.0\ M_{\odot}$, and $i = 27.1 \pm 0.8$ deg (Orosz et al. 2011).

Quite generally, even the uncertainties in the analytic Novikov-Thorne model are significantly less important than the uncertainties in D, M and i, as has been shown via GRMHD simulations of thin accretion disks (Section 5.1). In the case of Cygnus X-1, the model errors are especially small because of the extreme spin of the black hole and because of the low luminosity of the disk ($L/L_{\rm Edd} \approx 2\%$). Spin estimates obtained by fitting mock spectra of simulated GRMHD disks indicate that for an inclination $i = 30$ deg (which closely approximates the 27 deg inclination of Cygnus X-1), the Novikov-Thorne thin-disk model overestimates the spin parameter by only $\Delta a_* = 0.007$ and 0.005 for spins of 0.90 and 0.98, respectively (see Table 1 in Kulkarni et al. 2011). Furthermore, these errors are likely significantly overestimated because (1) they were computed for disks that are far more luminous ($L/L_{\rm Edd} \sim 0.35$), and hence thicker, than that of Cygnus X-1 ($L/L_{\rm Edd} \approx 0.02$), and (2) the deviations from the Novikov-Thorne model seem to increase as the luminosity, and hence disk thickness increases[18] (Kulkarni et al. 2011), as anticipated in previous work (Paczyński 2000; Shafee et al. 2008b). Thinner disks have not yet been simulated because to do so is computationally very challenging.

For the spin of Cygnus X-1, the effect of the uncertainty in the absolute flux calibration is very comparable to the 6% uncertainty in D, which is equivalent to a 12% uncertainty in the measurement of flux. We have therefore included in our error budget a 10% uncertainty in flux (Toor & Seward 1974), which we approximate as an uncertainty in the distance of 0.1 kpc, by simply combining the distance and flux-calibration errors in quadrature, thereby inflating the actual 0.120 kpc distance uncertainty to 0.156 kpc. Thus, the final error we report for a_* includes the uncertainties in D, M, i and the uncertainty in the absolute flux calibration. Taken together, these four sources of uncertainty totally dominate the error budget. (For a discussion of other lesser sources of error, see Section 5 and Appendix A in Steiner et al. 2011, and Section 5 in McClintock et al. 2013).

As in GOU11, in order to determine the error in a_* due to the combined uncertainties in D, M and i, we performed Monte Carlo simulations using the Odyssey computing cluster at Harvard University. The latter two parameters are not independent. They are related through the expression for the mass function: $f(M) \equiv M^3 \sin^3 i/(M + M_2)^2 = 0.263 \pm 0.004\ M_{\odot}$, where $M_2 = 19.16 \pm 1.90\ M_{\odot}$ is the mass of the secondary star and the value of the mass function was evaluated using a K-velocity of 76.79 ± 0.41 km s^{-1} and an orbital period of $P = 5.599829$ days (Orosz et al. 2011).

[18] In contrast, Noble et al. (2010) find that the stress profile is almost completely independent of disk thickness.

In the analysis, we assumed that the value of the mass function, the inclination, and the mass of the secondary are normally and independently distributed, and we computed the mass of the black hole using the values of these quantities, which are given above. We conservatively fixed the viscosity parameter at its baseline value, $\alpha = 0.1$ (using $\alpha = 0.01$ increases a_*; see Section 5.6). Specifically, we (i) generated 9000 parameter sets for D, i, M_2, and $f(M)$; (ii) solved for M for a given triplet of values of i, M_2 and $f(M)$; (iii) computed for each set the look-up table for the spectral hardening factor f using the model BHSPEC; and (iv) obtained a_* by fitting our adopted model to the spectra. The final histogram distributions for our six spectra and the corresponding 3σ lower limits on a_* are shown in Figure 5.

Were we to use these six limits to derive a joint constraint on spin, it would be more stringent than any one of the individual limits. We choose instead the conservative approach of adopting the most constraining *single* limit for our final result, namely, the limit for spectrum S3. *We therefore conclude that* $a_* > 0.983$ *at the* 3σ *limit of confidence*[19].

We note the following two caveats: First, we assume that the spin vector of the black hole is reasonably aligned with the orbital angular momentum vector (Section 5.8). Second, we assume that the asynchronous dynamical model is correct (see Section 7.3 in GOU11).

7. DISCUSSION

We first discuss two spin estimates for Cygnus X-1 made using the Fe-line method, which provide support for an extreme value of spin. We then relate Cygnus X-1 to the other members of its distinctive class of black-hole X-ray sources that are persistently bright.

7.1. *Measurement of Spin via the Fe-K/Reflection Method*

Two recent measurements of the spin of Cygnus X-1 obtained using X-ray reflection spectroscopy, aka the Fe line method (Reynolds 2013), support a high or extreme value of spin.

Duro et al. (2011) report $a_* = 0.88^{+0.07}_{-0.11}$. Their provisional result is based on an analysis of a single simultaneous observation made using *XMM-Newton* and *RXTE*. A limitation of their result is that it depends on assuming a single, fixed value of 3 for the emissivity index q, which is a canonical value. That is, they assume that the intensity of the flux irradiating the disk varies with radius as r^{-3}. When they allow q to vary freely, both the spin parameter and emissivity index are poorly constrained (see their Table 1). In short, their data are unable to determine both the profile of the illuminating radiation and the spin.

The result of Duro et al. (2011) is superseded by that of Fabian et al. (2012) who report $a_* = 0.97^{+0.014}_{-0.02}$. This result is based on an analysis of a single hard-state *Suzaku* spectrum. Fabian et al. describe this spectrum as "an average data set" (from a collection of 20 similar spectra) and report that consistent results were obtained for other data sets. The fit over a 1–500 keV band gives precise results for a 3-parameter, broken power-law model of the radial profile of the irradiating flux: Inside the break radius ($R_{\rm break} = 4.0 \pm 1.1\ GM/c^2$), $q > 6.8$, and outside $q = 2.75 \pm 0.15$. A strength of our work compared to that of Fabian et al., is the considerable attention we give to assessing the effects of a wide range of systematic errors, a topic that is not addressed in Fabian et al. (2012).

Earlier, Miller et al. (2009) reported a near-zero spin for Cygnus X-1, $a_* = 0.05 \pm 0.01$, based on an analysis of two *XMM-Newton* spectra. Neither Fabian et al. (2012) nor Duro et al. (2011) offer an explanation for this glaring discrepancy. However, recently an explanation was suggested for the near-zero spin reported by Miller et al. in terms of pile-up effects (see Section 4.3 in Reynolds 2013). This example shows that measurements of spin in the literature can be grossly affected by systematic effects, which should be carefully considered in assessing the reliability of spin results.

7.2. *Cygnus X-1 and the Other Persistent Black Hole Systems*

There are five dynamically established black-hole binaries containing wind-fed black holes and O-supergiant or Wolf-Rayet companions (Özel et al. 2010; McClintock et al. 2013); these systems are persistently X-ray bright. In the following, we do not consider the two systems with Wolf-Rayet companions, IC 10 X-1 and NGC 300 X-1, because the masses of their black holes are very uncertain and their spins have not been estimated. By contrast, the three remaining systems – Cygnus X-1, LMC X-1 and M33 X-7 – have well-determined values of both mass and spin. These fundamental data, which provide a *complete* description of these three black holes, appear in the two leftmost columns of Table 4.

While acknowledging that the sample is small, it appears that wind-fed black holes with supergiant companions are restricted to high spin, $a_* > 0.8$, in contrast with the broad distribution of spins observed for Roche-lobe-fed black holes with low or intermediate mass companions: four of them have low spins, $a_* \approx 0$, two have high spins, $a_* \sim 0.7 - 0.8$, and one has an extreme spin, $a_* > 0.95$ (see Table 1 in McClintock et al. 2013).

Not only are the persistent black holes all rapidly spinning, they are also relatively massive, $M = 11 - 16\ M_\odot$ (Table 4). By comparison, the masses of the transient black holes are significantly lower, and their mass distribution is remarkably narrow: $7.8 \pm 1.2\ M_\odot$ (Özel et al. 2010; Farr et al. 2011).

The data in Table 4 highlight a sharp and well-known distinction between the persistent systems and the transient systems, namely that the secondary stars in the former are far more massive, $M_2 = 20 - 70\ M_\odot$ (Table 4); they likewise have much higher temperatures, $30000 - 36000$ K (Orosz et al. 2007, 2009, 2011). The masses and temperatures of the secondaries in the transient systems are typically $< 1\ M_\odot$ and $4000 - 5000$ K; even in exceptional cases, their masses and temperatures are only $M_2 \lesssim 5\ M_\odot$ and $T_{\rm eff,2} \lesssim 15000$ K (Charles & Coe 2006). Finally, we note that for the persistent systems the radii of the secondaries and orbital periods fall in quite narrow ranges (Table 4), while the radii and periods for the transient systems are very broadly distributed, a distinction that is elegantly illustrated in Jerome Orosz's schematic sketch of 21 black hole binaries (see Figure 1 in McClintock et al. 2013).

The persistent black holes were very likely born with their high spins because their host systems are too young for the black holes to have had time to spin up via accretion torques (see Section 7.7 in GOU11 for details). The ages of Cygnus X-1, LMC X-1 and M33 X-7 are < 10 million years, whereas the spin-up times are $\gtrsim 17$ million years if one assumes the maximum, Eddington-limited accretion rate. Meanwhile, the spin-up times are likely much longer than 17 million years

[19] In GOU11, we conservatively adopted the spin limit for SP1 ($a_* > 0.95$) as our final result because it was the only one of the three spectra whose scattering fraction was $< 25\%$.

given that the systems are presently radiating at only $\sim 10\%$ of Eddington luminosity (Table 4).

The rotational energy of the persistent black holes is enormous, $\sim 2\ M_\odot c^2$ for LMC X-1 and M33 X-7 and $> 2.8\ M_\odot c^2$ for Cygnus X-1 (Christodoulou & Ruffini 1971)[20]. Correspondingly, a substantial fraction of the gravitational mass of these black holes is attributable to their rotational energy: $\sim 15\%$ for LMC X-1 and M33 X-7 and $> 19\%$ for Cygnus X-1.

8. CONCLUSION

In GOU11, while considering a wide range of systematic effects, including uncertainties in the Novikov-Thorne disk model, we concluded that the spin of the black hole in Cygnus X-1 is extreme: $a_* > 0.95$ (3σ). Unfortunately, the result was potentially biased by the relatively strong Compton component of emission, the strength of which can be characterized by the fraction $f_{\rm s}$ of thermal seed photons that are scattered into the power-law tail. The three spectra analyzed in GOU11 have $f_{\rm s} > 23\%$, while $f_{\rm s} \approx 25\%$ is the upper limit for reliable application of the continuum-fitting method (Steiner et al. 2009a). Subsequently, Fabian et al. (2012) employed the independent Fe-line method and confirmed that the spin of Cygnus X-1 is $a_* > 0.95$ (1σ); however, this result is less certain because systematic effects in the model have not been assessed.

Herein, we present a continuum-fitting analysis of six additional spectra, each of which confirms that $a_* > 0.95$ (3σ). This confirmation is compelling first because sources of systematic error have been thoroughly addressed (see Section 5 herein; Sections 5–7 in GOU11; McClintock et al. 2013). Secondly, and crucially, five of the spectra, S1–S5, are only moderately Comptonized with scattering fractions $f_{\rm s} = 10 - 19\%$, a regime where it has been firmly established that continuum-fitting results are reliable. This conclusion is based on studies of two black holes: (i) 33 spectra of H1743–322 with $\overline{f}_{\rm s} = 13.5\%$ (in the SPL state) each gave spins consistent with those obtained for dozens of thermal-state spectra ($\overline{f}_{\rm s} = 1\% - 7\%$; Steiner et al. 2009a); and (ii) 25 spectra of XTE J1550–564 with $\overline{f}_{\rm s} = 14.4\%$ each likewise gave spins consistent with those obtained for dozens of thermal-state spectra ($\overline{f}_{\rm s} = 2.3\%$; Steiner et al. 2011). In short, these two studies show that moderately Comptonized spectra with $f_{\rm s} \sim 15\%$, like S1–S5, give the same values of spin as spectra that are strongly disk-dominated with $f_{\rm s} \sim 1\% - 2\%$.

Our bottom line is that new and more reliable continuum spectra confirm the findings of GOU11 while establishing an even more stringent limit on the extreme spin of the black hole in Cygnus X-1: $a_* > 0.983$ at the 3σ (99.7%) level of confidence.

We are grateful to Director H. Tananbaum and Project Scientists T. Strohmayer and N. Gehrels for granting us respectively *Chandra*, *RXTE* and *Swift* observing time. We thank M. Nowak and N. Schulz for help in planning the *Chandra* observations; M. Nowak, J. Wilms and Bin-Bin Zhang for discussions on X-ray data analysis. We also thank S. Yamada for reducing the Suzaku data and J.G. Xiang for reducing the Chandra TE data. This research has made use of data obtained from the High Energy Astrophysics Science Archive Research Center (HEASARC) at NASA/Goddard Space Flight Center. LJG thanks the Harvard FAS Sciences Division Research Computing Group for their technical support on the Odyssey cluster. LJG acknowledges the support of NSFC grant (Y211541001) and NAOC grant (Y234031001), JEM acknowledges support from NASA grant NNX11AD08G, and MH acknowledges funding from the Bundesministerium für Wirtschaft und Technologie under grant number DLR 50 OR 0701.

[20] By comparison, the energy radiated by the Sun in its ~ 10 billion year lifetime is $\lesssim 0.001\ M_\odot c^2$.

REFERENCES

Arnaud, K. A. 1996, in Astron. Soc. of the Pac. Conf. Ser., Vol. 101, Astronomical Data Analysis Software and Systems V, ed. G. H. Jacoby & J. Barnes, 17, XSPEC is available at http://heasarc.gsfc.nasa.gov/xanadu/xspec/
Bardeen, J. M., Press, W. H., & Teukolsky, S. A. 1972, ApJ, 178, 347
Bolton, C. T. 1972, Nature, 240, 124
Bowyer, S., Byram, E. T., Chubb, T. A., & Friedman, H. 1965, Science, 147, 394
Brenneman, L. W. & Reynolds, C. S. 2006, ApJ, 652, 1028
Canizares, C. R. et al. 2005, PASP, 117, 1144
Charles, P. A. & Coe, M. J. 2006, Optical, ultraviolet and infrared observations of X-ray binaries, ed. W. H. G. Lewin & M. van der Klis, 215–265
Christodoulou, D. & Ruffini, R. 1971, Phys. Rev. D, 4, 3552
Dauser, T., Wilms, J., Reynolds, C. S., & Brenneman, L. W. 2010, MNRAS, 409, 1534
Davis, S. W., Blaes, O. M., Hubeny, I., & Turner, N. J. 2005, ApJ, 621, 372
Davis, S. W. & Hubeny, I. 2006, ApJS, 164, 530
Dickey, J. M. & Lockman, F. J. 1990, ARA&A, 28, 215
Duro, R. et al. 2011, A&A, 533, L3
Fabian, A. C. et al. 2012, MNRAS, 424, 217
Farr, W. M., Sravan, N., Cantrell, A., Kreidberg, L., Bailyn, C. D., Mandel, I., & Kalogera, V. 2011, ApJ, 741, 103
García, J., Dauser, T., Reynolds, C. S., Kallman, T. R., McClintock, J. E., Wilms, J., & Eikmann, W. 2013, ApJ, 768, 146
Garmire, G. P., Bautz, M. W., Ford, P. G., Nousek, J. A., & Ricker, Jr., G. R. 2003, in Presented at the Society of Photo-Optical Instrumentation Engineers (SPIE) Conference, Vol. 4851, Society of Photo-Optical Instrumentation Engineers (SPIE) Conference Series, ed. J. E. Truemper & H. D. Tananbaum, 28–44
Gou, L. et al. 2009, ApJ, 701, 1076
— 2011, ApJ, 742, 85
Hanke, M., Wilms, J., Nowak, M. A., Barragán, L., & Schulz, N. S. 2010, A&A, 509, L8
Hanke, M., Wilms, J., Nowak, M. A., Pottschmidt, K., Schulz, N. S., & Lee, J. C. 2009, ApJ, 690, 330
Kalberla, P. M. W., Burton, W. B., Hartmann, D., Arnal, E. M., Bajaja, E., Morras, R., & Pöppel, W. G. L. 2005, A&A, 440, 775
Karitskaya, E. A. et al. 2007, Astronomical and Astrophysical Transactions, 26, 159
King, A. R., Pringle, J. E., & Livio, M. 2007, MNRAS, 376, 1740
Kulkarni, A. K. et al. 2011, MNRAS, 414, 1183
Li, L., Zimmerman, E. R., Narayan, R., & McClintock, J. E. 2005, ApJS, 157, 335
Liu, J., McClintock, J. E., Narayan, R., Davis, S. W., & Orosz, J. A. 2008, ApJ, 679, L37, Erratum: 2010, ApJ, 719, L109
McClintock, J. E., Narayan, R., & Steiner, J. F. 2013, arXiv:1303.1583v1
McClintock, J. E. & Remillard, R. A. 2006, Black hole binaries, ed. W. H. G. Lewin & M. van der Klis, 157–213
McClintock, J. E., Shafee, R., Narayan, R., Remillard, R. A., Davis, S. W., & Li, L. 2006, ApJ, 652, 518
Mihara, T. et al. 2011, PASJ, 63, 623
Miller, J. M., Reynolds, C. S., Fabian, A. C., Miniutti, G., & Gallo, L. C. 2009, ApJ, 697, 900
Mirabel, I. F. & Rodrigues, I. 2003, Science, 300, 1119
Noble, S. C., Krolik, J. H., & Hawley, J. F. 2010, ApJ, 711, 959
Noble, S. C., Krolik, J. H., Schnittman, J. D., & Hawley, J. F. 2011, ApJ, 743, 115
Novikov, I. D. & Thorne, K. S. 1973, in Black Holes (Les Astres Occlus), ed. C. Dewitt & B. S. Dewitt, 343–450

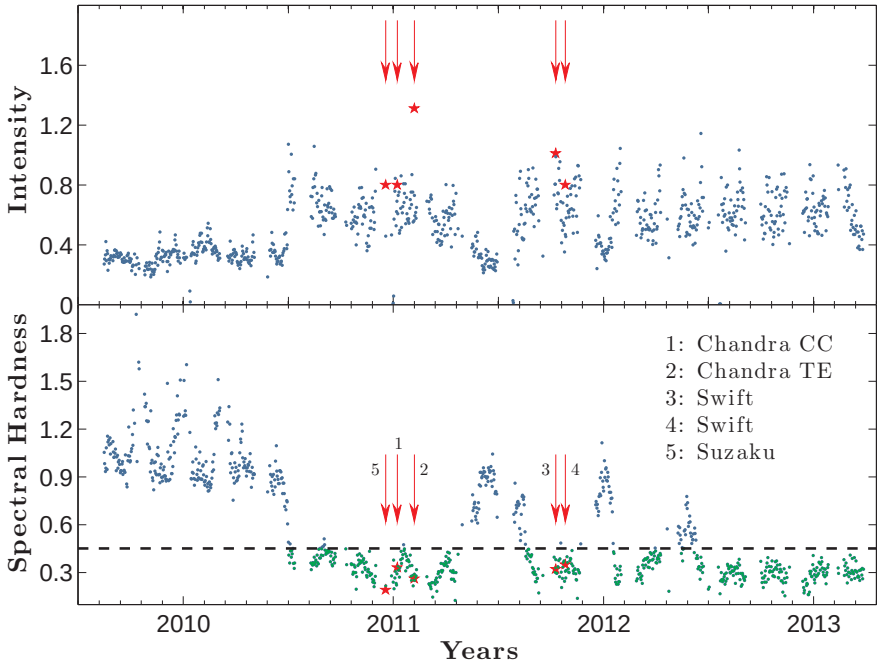

Figure 1. Four-year record for Cygnus X-1 of the 2–10 keV X-ray intensity relative to the Crab Nebula (top) and spectral hardness (bottom) based on data obtained using the MAXI Gas Slit Camera (GSC; Mihara et al. 2011). The hardness is defined as the ratio of counts detected in a hard X-ray band (4–10 keV) to those detected in a soft band (2–4 keV). We consider data suitable for the measurement of spin only when the spectral hardness is below the dashed line (SH < 0.45), which is an empirical choice. Shown plotted as red stars are the intensity and hardness of the source as observed by MAXI on the days of the five observations listed in Table 1. While a useful diagnostic for the purposes of data selection, these survey data are unsuitable for the measurement of spin.

Orosz, J. A., McClintock, J. E., Aufdenberg, J. P., Remillard, R. A., Reid, M. J., Narayan, R., & Gou, L. 2011, ApJ, 742, 84
Orosz, J. A. et al. 2007, Nature, 449, 872
— 2009, ApJ, 697, 573
Özel, F., Psaltis, D., Narayan, R., & McClintock, J. E. 2010, ApJ, 725, 1918
Paczyński, B. 2000, arXiv:astro-ph/0004129v1
Penna, R. F., McKinney, J. C., Narayan, R., Tchekhovskoy, A., Shafee, R., & McClintock, J. E. 2010, MNRAS, 408, 752
Predehl, P. & Schmitt, J. H. M. M. 1995, A&A, 293, 889
Reid, M. J., McClintock, J. E., Narayan, R., Gou, L., Remillard, R. A., & Orosz, J. A. 2011, ApJ, 742, 83
Remillard, R. A. & McClintock, J. E. 2006, ARA&A, 44, 49
Reynolds, C. S. 2013, ArXiv e-prints
Romano, P. et al. 2006, A&A, 456, 917
Ross, R. R., Fabian, A. C., & Young, A. J. 1999, MNRAS, 306, 461
Shafee, R., McKinney, J. C., Narayan, R., Tchekhovskoy, A., Gammie, C. F., & McClintock, J. E. 2008a, ApJ, 687, L25
Shafee, R., Narayan, R., & McClintock, J. E. 2008b, ApJ, 676, 549
Smith, R. K., Edgar, R. J., & Shafer, R. A. 2002, ApJ, 581, 562
Steiner, J. F., McClintock, J. E., & Reid, M. J. 2012, ApJ, 745, L7
Steiner, J. F., McClintock, J. E., Remillard, R. A., Gou, L., Yamada, S., & Narayan, R. 2010, ApJ, 718, L117
Steiner, J. F., McClintock, J. E., Remillard, R. A., Narayan, R., & Gou, L. 2009a, ApJ, 701, L83
Steiner, J. F., Narayan, R., McClintock, J. E., & Ebisawa, K. 2009b, PASP, 121, 1279
Steiner, J. F. et al. 2011, MNRAS, 416, 941
Thorne, K. S. 1974, ApJ, 191, 507
Toor, A. & Seward, F. D. 1974, AJ, 79, 995
Webster, B. L. & Murdin, P. 1972, Nature, 235, 37
Wilms, J., Allen, A., & McCray, R. 2000, ApJ, 542, 914
Xiang, J., Lee, J. C., Nowak, M. A., & Wilms, J. 2011, ApJ, 738, 78
Yamada, S. et al. 2013, ApJ, 767, L35
— 2012, PASJ, 64, 53
Zhang, S. N., Cui, W., & Chen, W. 1997, ApJ, 482, L155
Zhu, Y., Davis, S. W., Narayan, R., Kulkarni, A. K., Penna, R. F., & McClintock, J. E. 2012, MNRAS, 424, 2504

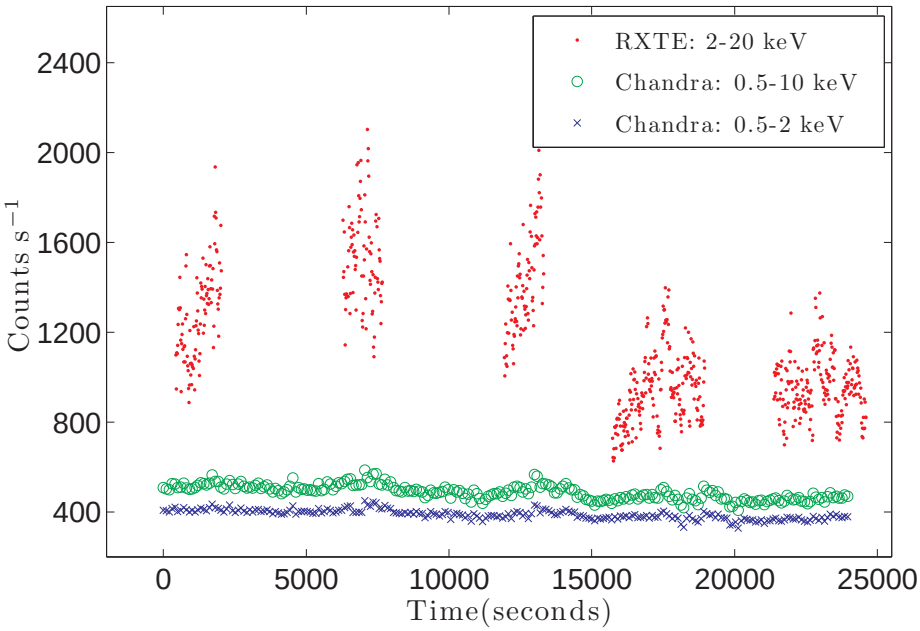

Figure 2. *RXTE* and *Chandra* count rates in the energy bands indicated for Observation No. 1. The strictly simultaneous segments of data used to produce the five spectra of highest quality, namely S1–S5, correspond in the figure to the five time intervals defined by the five clusters of *RXTE* data points (red filled circles). The UT start and stop times of each of these five time intervals are given in Table 1. Note the strong variability in the *RXTE* band, where the Compton component dominates, relative to the *Chandra* bands, where the thermal component dominates.

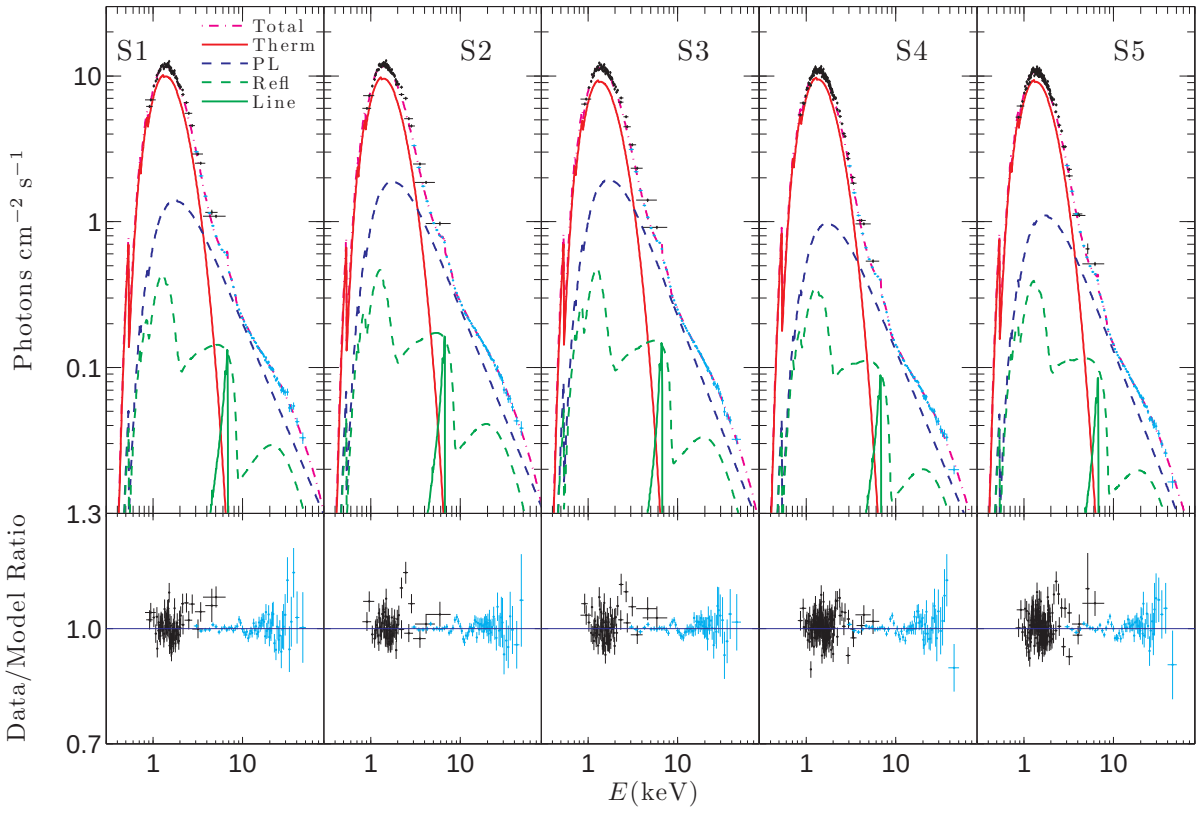

Figure 3. (**Top**) The upper envelope in each of these spectra shows the data (*RXTE* in blue, and *ASCA* or *Chandra* in black) and the best-fit model. Each total model spectrum is shown decomposed into thermal and power-law components, and a reflection component, which is comprised of a continuum component plus the F Kα line feature. (The color assignments correspond to those used in Figure 2 in GOU11.) The low-energy X-ray absorption component is evident at energies $\lesssim$1 keV. Note in all three spectra the dominance at low energies of the key thermal component. (**Bottom**) Ratio of the data to the model showing deviations between the two.

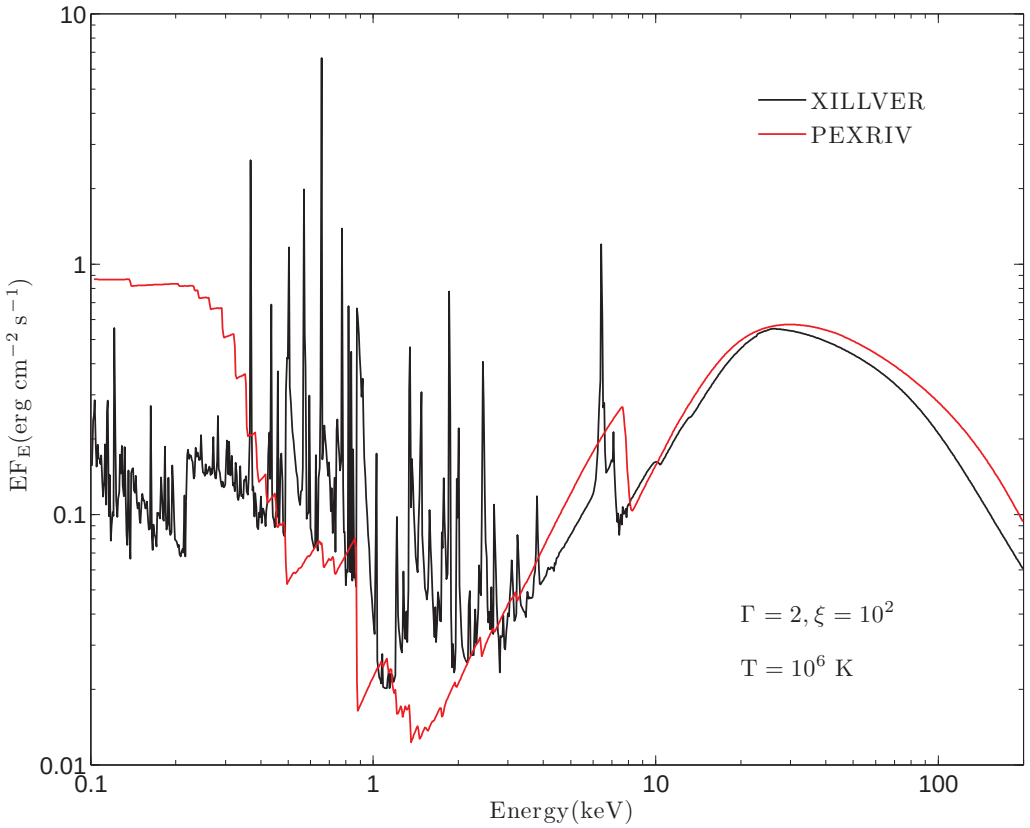

Figure 4. Comparison of reflected spectra computed using the advanced model XILLVER (black curve with emission lines) and using PEXRIV (red curve) for a power-law spectrum with photon index $\Gamma = 2$ incident on an optically-thick slab of gas; the ionization parameter in this example, $\xi = 100$, is a good match to the values observed for Cygnus X-1. This figure was computed by J. Garcia in precisely the same way as the pair of figures shown in Figure 20 in García et al. (2013). The disk temperature in the PEXRIV model is set to its maximum possible value, $T = 10^6$K; the high-energy cutoff is 300 keV; and the abundances are assumed to be solar. The large discrepancies between the two models at $E < 0.4$ keV have no bearing on our results because the detectors do not respond at these low energies (Table 1). The obvious discrepancy between the models in the vicinity of the Fe K complex is the origin of the residual feature near 9 keV (Section 5.2; Figure 3).

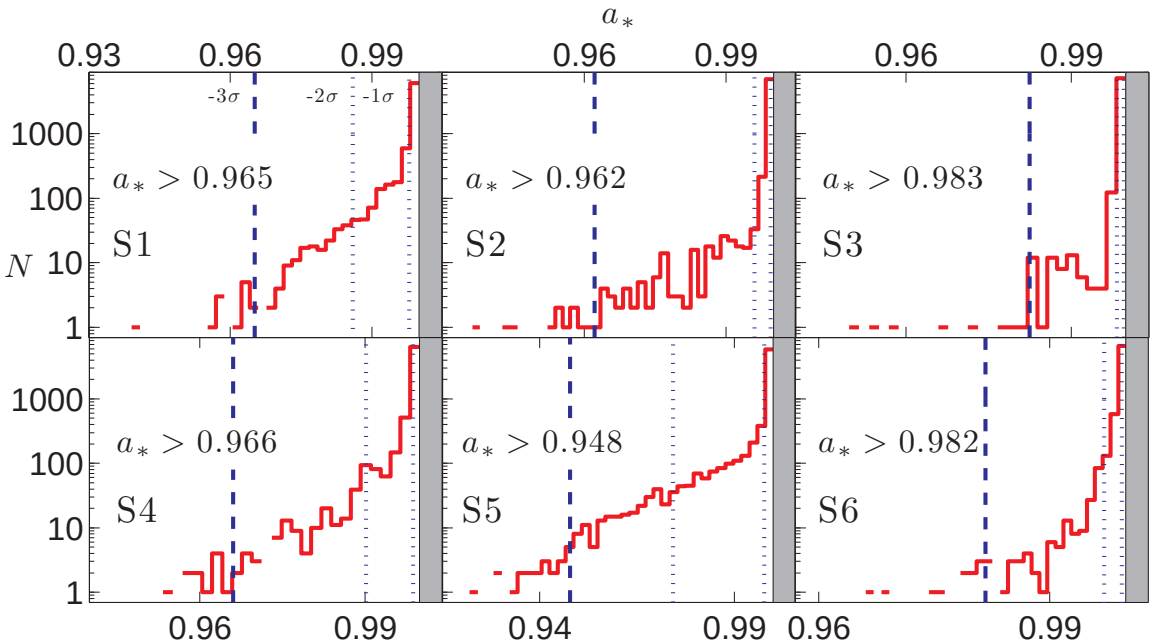

Figure 5. Histograms of a_* for 9000 parameter sets (per spectrum) resulting from the Monte Carlo analysis of the selected spectra with scattering fractions $f_s < 25\%$. The lower limits given are at the 3σ (99.7%) level of confidence.

Table 1
Journal of the observations[a]

Obs. No.	Spec. No.	Mission	Detector	$E1$-$E2$ (keV)	UT	$T_{\rm exp}$ (sec)	I (Crab)	SH	ϕ
1	S1	*Chandra & RXTE*	HETG(CC) & PCA	0.8-8.0 & 2.9-50	2011-01-06 14:06:40–14:35:44	455 & 1744	0.52	0.24	0.32
1	S2	*Chandra & RXTE*	HETG(CC) & PCA	0.8-8.0 & 2.9-50	2011-01-06 15:44:16–16:09:52	398 & 1536	0.61	0.44	0.33
1	S3	*Chandra & RXTE*	HETG(CC) & PCA	0.8-8.0 & 2.9-50	2011-01-06 17:15:28–17:43:44	462 & 1696	0.57	0.33	0.35
1	S4	*Chandra & RXTE*	HETG(CC) & PCA	0.8-8.0 & 2.9-50	2011-01-06 18:19:44–19:17:52	997 & 3488	0.38	0.26	0.36
1	S5	*Chandra & RXTE*	HETG(CC) & PCA	0.8-8.0 & 2.9-50	2011-01-06 19:53:36–20:50:08	847 & 3392	0.38	0.22	0.37
2	S6	*Chandra & RXTE*	HETG(TE) & PCA	0.5-10.0 & 2.9-50	2011-02-05 07:02:00–09:37:00	3593 & 3600	0.58	0.25	0.64
2	S7	*Chandra & RXTE*	HETG(TE) & PCA	0.5-10.0 & 2.9-50	2011-02-05 10:10:00–10:31:00	929 & 1232	0.74	0.31	0.65
3	S8	*Swift & RXTE*	XRT(WT) & PCA	0.5-10.0 & 2.9-50	2011-10-08 20:03:28–20:26:08	1355 & 1344	0.59	0.32	0.48
3	S9	*Swift & RXTE*	XRT(WT) & PCA	0.5-10.0 & 2.9-50	2011-10-08 21:40:00–22:02:08	1326 & 1328	0.90	0.28	0.49
4	S10	*Swift & RXTE*	XRT(WT) & PCA	0.5-10.0 & 2.9-50	2011-10-26 03:28:00–04:10:00	1454 & 2464	0.47	0.35	0.57
5	S11	*Suzaku*	XIS & HXD	0.5-10.0 & 2.5-45	2010-12-17 14:31:07–18:49:22	868	-	0.19	0.77

[a] For five observations, yielding 11 data segments and 11 corresponding spectra (S1–S11), in columns 3–10 we give the following information: names of the observatories; names of the detectors employed with the data mode indicated in parentheses; bandwidths used in the analysis; UT start and ending times of the observations; effective exposure times for the corresponding detectors; the source intensity; spectral hardness (SH); and orbital phase during the observation. The orbital phase of the binary system is defined (at the midpoint of the observation) relative to the time of supergiant superior conjunction (black hole beyond O-star), which occurred on heliocentric Julian Day 2441163.529 (Orosz et al. 2011).

Table 2
Fit Results for Observation No. 1: Spectra S1-S5[a]

Number	Model	Parameter	S1	S2	S3	S4	S5
1	KERRBB2	a_*	$0.99990^{+0.00000\,\rm b}_{-0.00877}$	$0.99990^{+0.00000\,\rm b}_{-0.00872}$	$0.99990^{+0.00000\,\rm b}_{-0.00838}$	$0.99990^{+0.00000\,\rm b}_{-0.00545}$	$0.99950^{+0.00013\,\rm b}_{-0.00348}$
2	KERRBB2	$\dot{M}$	0.119 ± 0.013	0.121 ± 0.013	0.116 ± 0.012	0.108 ± 0.007	0.113 ± 0.005
3	const	–	0.7819 ± 0.0074	0.6257 ± 0.0075	0.7534 ± 0.0073	0.7566 ± 0.0055	0.7518 ± 0.0065
4	TBABS	$N_{\rm H}$	0.7777 ± 0.0141	0.7806 ± 0.0141	0.7597 ± 0.0136	0.7357 ± 0.0088	0.7564 ± 0.0072
5	SIMPLR	Γ	2.4438 ± 0.0094	2.4906 ± 0.0098	2.5753 ± 0.0094	2.4662 ± 0.0081	2.5751 ± 0.0081
6	SIMPLR	$f_{\rm SC}$	0.1347 ± 0.0027	0.1783 ± 0.0034	0.1924 ± 0.0033	0.1022 ± 0.0015	0.1195 ± 0.0016
7	KERRDISK	$E_{\rm L}$	6.571 ± 0.036	6.482 ± 0.059	6.446 ± 0.048	6.560 ± 0.032	6.466 ± 0.036
8	KERRDISK	q	2.559 ± 0.051	2.456 ± 0.082	2.384 ± 0.062	2.595 ± 0.042	2.398 ± 0.045
9	KERRDISK	$N_{\rm L}$	0.020 ± 0.001	0.023 ± 0.002	0.018 ± 0.001	0.014 ± 0.001	0.012 ± 0.000
10	KERRDISK	EW	0.283	0.238	0.211	0.292	0.228
11	IREFLECT[c]	[Fe]	5.4269 ± 0.4637	3.9534 ± 0.2995	4.3540 ± 0.3139	4.7329 ± 0.3721	3.7402 ± 0.2688
12	IREFLECT	ξ	140.0 ± 13.2	94.3 ± 11.6	87.9 ± 8.7	166.0 ± 13.2	121.6 ± 8.7
13		χ^2_ν	0.95(595/628)	0.95(545/573)	0.97(605/625)	1.20(890/745)	1.12(1119/998)
14		f	1.60	1.62	1.62	1.61	1.61
15		$L/L_{\rm Edd}$	0.022	0.022	0.022	0.020	0.019
16	ADOPTED	a_*[d]	$0.99990^{+0.00000}_{-0.00877}$	$0.99990^{+0.00000}_{-0.00872}$	$0.99990^{+0.00000}_{-0.00838}$	$0.99990^{+0.00000}_{-0.00545}$	$0.99950^{+0.00013}_{-0.00348}$

[a] For the model components given, the parameters from top to bottom are: (1) spin parameter; (2) mass accretion rate in units of 10^{18} g s^{-1}; (3) detector normalization constant relative to *RXTE* PCU2; (4) hydrogen column density in units of 10^{22} cm^{-2}; (5) photon power-law index Γ; (6) scattering fraction $f_{\rm s}$; (7) central line energy in keV; (8) emissivity index q; (9) line flux in units of photons cm^{-2} s^{-1}; (10) equivalent width of line in keV; (11) iron abundance relative to solar; (12) ionization parameter ξ; (13) Reduced chi-square, total chi-square and degrees of freedom, respectively; (14) spectral hardening factor f; and (15) Eddington-scaled disk luminosity, where $L_{Edd} \approx 1.9 \times 10^{39}$ erg s^{-1} for Cygnus X-1. Unless otherwise indicated, the uncertainties quoted here and throughout the paper are at the 1σ level of confidence.
[b] Although the physical maximum value of the spin parameter for disk accretion is $a_* \approx 0.998$ (Thorne 1974), the formal maximum value for the XSPEC model KERRBB2 is 0.9999. The errors quoted here, which were computed using the command *error* in XSPEC, are the uncertainties due to counting statistics only.
[c] The scaling factor s in the model IREFLECT was set to unity for all fits (see text).
[d] Final adopted values for the spin parameter and their uncertainties. The 1σ uncertainties are calculated based on the 3σ lower limits on a_* shown in Figure 5. These results fold in the uncertainties in D, M, i, and the absolute flux calibration via our Monte Carlo analysis (see Section 6).

Table 3
Fit Results for Observations 2–4: Spectra S6–S10

Number	Model	Parameter	S6	S7	S8	S9	S10
1	KERRBB2	a_*	$0.99990^{+0.00000}_{-0.00922}$	$0.97177^{+0.00938}_{-0.00450}$	$0.99990^{+0.00000}_{-0.00520}$	$0.99988^{+0.00001}_{-0.00546}$	$0.99990^{+0.00000}_{-0.00842}$
2	KERRBB2	$\dot{M}$	0.115 ± 0.013	0.194 ± 0.008	0.113 ± 0.007	0.128 ± 0.008	0.108 ± 0.011
3	const	–	0.8989 ± 0.0379	0.7259 ± 0.0797	1.2432 ± 0.0116	1.3873 ± 0.0085	1.8046 ± 0.0191
4	TBABS	$N_{\rm H}$	0.7148 ± 0.0103	0.7241 ± 0.0182	0.7875 ± 0.0062	0.7527 ± 0.0054	0.7911 ± 0.0098
5	SIMPLR	Γ	2.6976 ± 0.0062	2.7430 ± 0.0079	2.6248 ± 0.0088	2.6649 ± 0.0071	3.0264 ± 0.0162
6	SIMPLR	$f_{\rm s}$	0.2359 ± 0.0041	0.2942 ± 0.0058	0.2927 ± 0.0038	0.4800 ± 0.0111	0.3118 ± 0.0077
7	KERRDISK	$E_{\rm L}$	6.514 ± 0.026	6.531 ± 0.036	6.545 ± 0.072	6.516 ± 0.046	6.539 ± 0.049
8	KERRDISK	q	2.293 ± 0.049	2.152 ± 0.081	2.923 ± 0.061	2.467 ± 0.058	2.233 ± 0.107
9	KERRDISK	$N_{\rm L}$	0.017 ± 0.001	0.017 ± 0.001	0.016 ± 0.002	0.023 ± 0.001	0.011 ± 0.001
10	KERRDISK	EW	0.190	0.141	0.176	0.146	0.187
11	IREFLECT	[Fe]	4.0832 ± 0.1660	3.4452 ± 0.1602	4.2666 ± 0.4452	3.2580 ± 0.1721	1.3208 ± 0.1606
12	IREFLECT	ξ	74.3 ± 5.2	42.8 ± 5.0	220.4 ± 24.9	66.5 ± 6.2	82.3 ± 14.6
13		χ^2_ν	1.40(491/352)	1.61(323/201)	1.37(484/353)	1.54(612/399)	1.24(416/337)
14		f	1.60	1.59	1.59	1.60	1.59
15		$L/L_{\rm Edd}$	0.021	0.021	0.021	0.024	0.020
16	ADOPTED	a_*	$0.99990^{+0.00000}_{-0.00922}$	–	–	–	–

[a] Layout and parameter definitions are exactly the same as for Table 2.

Table 4
Data for Three Persistent Black Hole Binaries

Source[a]	a_*	$M(M_\odot)$	$M_2(M_\odot)$	P(days)	$L/L_{\rm Edd}$	References
Cygnus X-1	> 0.95	14.8 ± 1.0	19.2 ± 1.9	5.60	0.02	Gou et al. 2011; Orosz et al. 2011
LMC X-1	$0.92^{+0.05}_{-0.07}$	10.9 ± 1.4	31.8 ± 3.5	3.91	0.16	Gou et al. 2009; Orosz et al. 2009
M33 X-7	0.84 ± 0.05	15.7 ± 1.5	70.0 ± 6.0	3.45	0.09	Liu et al. 2008; Orosz et al. 2007

[a] From the left to the right, the parameters are, respectively, spin parameter, black hole mass, mass of the secondary, orbital period, and the Eddington-scaled disk luminosity.